1995

Performance Evaluation of an Axially Viewed Horizontal Inductively-Coupled Plasma for Optical-Emission Spectrometry

JC IVALDI

JF Tyson

Performance evaluation of an axially viewed horizontal inductively coupled plasma for optical emission spectrometry☆

Juan C. Ivaldi[a,*], Julian F. Tyson[b]

[a]*The Perkin-Elmer Corporation, 761 Main Avenue, Norwalk, CT 06859-0293, USA*

[b]*Department of Chemistry, The University of Massachusetts, Box 34510, Lederle Graduate Research Towers, Amherst, MA 01003-4510, USA*

Received 18 January 1995; accepted 2 March 1995

Abstract

A performance evaluation of a horizontal axially viewed inductively coupled plasma (ICP) for optical emission spectrometry is presented. The main contribution of this work is the elucidation of the sources of analytical performance differences using practical diagnostics in the comparison of axial and conventional radial viewing of the ICP. Figures of merit such as detection limit, background equivalent concentration, precision, and dynamic range are compared for both viewing arrangements. The detection limit improvements with axial viewing, known from previous work in the literature, are shown to be understood in the context of the signal-to-background-ratio relative-standard-deviation-of-the-background (SBR-RSDB) theory. The usefulness of the SBR-RSDB approach as a diagnostic tool for understanding the detection limit improvement and identifying performance differences is demonstrated. This approach can be further utilized for quality control and quality assurance of instrument performance and detection limit results. Other characteristic differences between axial and radial viewing are presented including matrix effects on line signals and the magnitudes of spectral interferences from OH bands. An overall improvement factor of five in detection power was observed when using axial viewing compared with radial viewing.

Keywords: ICP; ICP–OES; Optical emission spectrometry

1. Introduction

The detection limit advantages of the axially viewed inductively coupled plasma (ICP) for atomic emission spectrometry have been reported in the literature [1–8]. The first such publication came from the laboratory of Mermet and Robin [1] in which a detection limit comparison of axial and radial viewing was provided. Detection limit improvements up to a factor of five were observed for several elements. Much of the work reported in the literature contains results which are in agreement about the influence of axial viewing on certain analytical figures of

* Corresponding author.

☆ This manuscript contains material presented at the FACSS 1994 Conference in St. Louis.

merit. Specifically, there is general agreement that a five- to ten-fold improvement in detection power is obtained for axial viewing compared to conventional radial viewing of the ICP. The literature reports emphasized the increase in analyte signal owing to the longer pathlength with axial viewing. In general, self-absorption resulting in non-linearity of the working curve was found to occur at lower concentrations with axial viewing than with radial viewing. However, the linear dynamic range was reported to be similar with an overall shift to lower concentration. Conflicting conclusions have been presented concerning chemical matrix effects and the magnitude of the molecular and argon continuum background emission [2–8]. The discrepancies were probably the result of differences in experimental setups such as plasma source conditions, the torch and load coil geometry, the sample introduction system used, implementation of a shearing gas, etc. Some of these factors will be discussed.

There is no previous report of the use of axial viewing with ICP instrumentation having solid-state detection. In the existing literature, detection limit differences between radial and axial viewing have not been accounted for with a view towards rationalization of the differences using the same experimental protocol. In this work, experiments were conducted to investigate the performance of an axially viewed ICP coupled with an echelle spectrometer with matched segmented array solid-state detectors [9,10]. The focus of this work was on the evaluation of the performance of the axially viewed ICP using diagnostic methods such as the signal-to-background-ratio relative-standard-deviation-of-the-background (SBR-RSDB) approach for the calculation of detection limits [18,19]. Also used were the diagnostic line sets recommended by Mermet and co-workers [11–13].

The terminology used in the literature has not been entirely consistent with reference to the two viewing modes. For clarification, "axial" viewing is synonymous with "end-on" viewing and refers to the orientation in which the optical axis is coincident with the central channel. "Radial" viewing is synonymous with "side-on" or "lateral" viewing which is the conventional ICP viewing mode in which the optical axis is orthogonal to the central channel.

2. Experimental

2.1. Experimental conditions

The experimental conditions are summarized in Table 1. All solutions were prepared in aqueous media. The four sets of conditions were given names which identify important differences in some of the figures and tables. The names used were "radial" for Set 1, "axial" for Set 2, "axial robust" for Set 3, and "axial USN" for Set 4. Although four different sets of conditions were used, the same physical spectrometer, detectors and torch glassware geometry were used for all experiments. Using the same spectrometer facilitated comparisons of the detection limits and other parameters because the spectral bandpass function and the photo-

Table 1
Experimental conditions

	Set 1	Set 2	Set 3	Set 4
Instrument	Optima 3000	Optima 3000-XL	Optima 3000-XL	Optima 3000-XL
Viewing mode	Radial	Axial	Axial	Axial
RF power/W	950	950	1450	950
Nebulizer gas flow[a]	0.95	0.95	0.60	0.95
Auxiliary gas flow	1.0	1.0	1.0	1.0
Plasma gas flow	15	15	15	15
Viewing height[b]	15	NA[c]	NA[c]	NA[c]
Solution flow rate [d]	1.5	1.5	2	1.5
Nebulizer type	Sapphire-tipped cross-flow	Sapphire-tipped cross-flow	Modified conespray[e]	Ultrasonic

[a] All gas flows are for Ar in l min^{-1}. [b] Units of mm above the load coil. [c] NA, not applicable. [d] Units of ml min^{-1}. [e] See text for details.

metric efficiency of the system remained constant throughout the experiments. For all experiments, the normal spectral resolution mode of the spectrometer with the 62 μm slit [9] was used.

The term "robust", introduced by Mermet [11], used to describe Set 3 experimental conditions throughout the Discussion section, refers to the use of lower nebulizer gas flow rates and higher radio frequency (RF) powers. The benefits of using these conditions are the improved characteristics with respect to matrix effects arising from high levels of concomitants such as a high content of alkali elements. For the experiments performed under robust conditions, a special version of the Conespray nebulizer [14,15] was used which had a gas orifice diameter of 178 μm. The diameter permitted the use of the lower 0.6 l/min^{-1} gas flow-rate while maintaining consistent nebulizer operation.

For axial viewing, comparisons were made between pneumatic nebulization (Set 2 conditions) and ultrasonic nebulization (Set 4 conditions). When the ultrasonic nebulizer was used, the aerosol from the output of the Cetac U5000-AT unit was connected directly to the injector adapter at the base of the torch using Tygon tubing. The desolvation system temperatures used were 140°C for the heater and 0°C for the chiller.

2.2. *Instrumentation*

The instrumentation was very similar to that described previously [9,10]. There were three main differences between the radial and axial torch arrangements. First, the conventional radial ICP torch was oriented vertically with the optical axis at right angles to the central channel of the ICP whereas the axial torch was oriented horizontally with the optical axis coincident with the central channel. Thus, the appearance of the sample introduction and torch assembly for the axial setup resembled that which is typically used for inductively coupled plasma mass spectrometry (ICP–MS) instrumentation. An advantage of this arrangement was that the position of the optical axis and the positions of optical components in the transfer optics remained the same with either radial or axial viewing.

The second major difference was a modification to a mirror in the transfer optics. The modification resulted in sharp imaging of the central channel for axial viewing compared to the astigmatic viewing system used for radial viewing [9]. The cross-sectional diameter of the roughly cylindrical region in the torch which becomes imaged was about 1–2 mm so as to match the geometry of the axial channel of the ICP. This beam shape was important to avoid entrance of excess, off-axis background radiation into the spectrometer. The first mirror in the transfer optics had a computer driven two-axis motor drive which was used to automatically find the optimum viewing location.

The third difference between the radial and axial torches was that a plasma shearing gas flow was used with the axial system. The shearing gas was a thin curtain of air formed using a nozzle having a narrow 0.075 mm by 30 mm slot. The shearing gas flow was directed at right angles to the axis of the ICP and served two purposes: (1) it redirected relatively cooler analyte species in the plume out of the optical axis where they might have absorbed useful radiation or contributed to self-absorption, and (2) it kept the optical purge interface from coming into contact with hot plasma exhaust gases. The optical purge interface is a ceramic cone which extends the nitrogen purge along the optical axis. Useful positions for the shearing gas nozzle were found to be in the range between 29 and 34 mm beyond the load coil. This coincided with the region identified by Demers [3] as the visible boundary between the normal analytical zone and the plume when introducing high concentrations of yttrium.

2.3. *Data processing*

Multicomponent spectral fitting (MSF) data processing was used for all precision and detection limit experiments. Details of MSF have been presented elsewhere [16,17]. For precision measurements, a solution was prepared containing 20 μg ml^{-1} Zn, 1 μg ml^{-1} Mg, 0.5 μg ml^{-1} Ba and 2% nitric acid. This solution was also used for production of the analyte model spectra for the MSF routine. Models of the blank were collected using a 2% nitric acid solution. The relative standard deviations were calculated from 20 replicate measurements of the analyte

Table 2
Multielement detection limit data for Set 1 conditions, radial viewing with pneumatic nebulization; an integration time of 10 s was used

Element	λ/nm	DL/(ng ml^{-1})[a]	z_a[b]	z_b[c]	BEC/(ng ml^{-1})[d]	RSDB/%[e]
As	189.042	35	88	31.4	554	2.07
As	193.696	32	139	43.7	457	2.35
Ba	455.403	0.066	303480	5895	19.8	0.11
Be	313.042	0.071	155897	2331	15.2	0.15
Cd	214.438	1.3	2466	80.3	33.7	1.33
Cr	205.552	2.8	1069	64.2	63.9	1.47
Cu	324.754	0.73	16576	1272	83.1	0.29
Fe	238.204	2.4	1716	128	80.7	1.00
Mn	257.610	0.38	12847	195	15.4	0.82
Mo	202.030	2.9	912	63.2	74.4	1.30
Na	589.592	9.9	10441	4522	764	0.43
Ni	221.647	6.4	566	68.6	138	1.54
Pb	220.353	7.7	486	146	431	0.60
Sb	206.833	24	128	41.1	474	1.67
Se	196.026	39	61	32.9	680	1.91
Ti	334.941	0.36	23956	1001	43.6	0.27
U	367.007	3.3	5250	1278	322	0.34
V	309.311	0.96	14912	953	68.3	0.47
Zn	213.856	0.78	4645	93.7	20.6	1.26

[a] DL is the 3σ detection limit. [b] z_a is the peak intensity of the analyte plus the background contribution in counts s^{-1}. [c] z_b is the net background intensity at the wavelength of peak maximum in counts s^{-1}. [d] BEC is the background equivalent concentration. [e] RSDB is the relative standard deviation of the background, calculated using Eq. (1).

signal. The concentrations of the analytes were high enough so that the background contribution was negligible and the precision values were dominated by the flicker noise in the line signals.

For detection limit measurements, the analyte model spectra were collected using a solution containing 1 μg ml^{-1} of the elements listed in Tables 2–5, except for Se which was prepared at a concentration of 0.58 μg ml^{-1}. As in the precision work, a 2% nitric acid solution was

Table 3
Multielement detection limit data for Set 2 conditions, axial viewing with pneumatic nebulization; an integration time of 10 s was used[a]

Element	λ/nm	DL/(ng ml^{-1})	z_a	z_b	BEC/(ng ml^{-1})	RSDB/%
As	189.042	9.8	716	180	336	0.98
As	193.696	6.9	1462	354	319	0.72
Ba	455.403	0.010	4097686	22871	5.6	0.06
Be	313.042	0.026	3452357	72470	21	0.04
Cd	214.438	0.29	23567	636	28	0.35
Cr	205.552	0.41	5964	593	110	0.12
Cu	324.754	0.32	204179	9097	47	0.23
Fe	238.204	0.36	28724	994	36	0.33
Mn	257.610	0.055	223031	1539	6.9	0.26
Mo	202.030	0.63	13994	590	44	0.48
Na	589.592	0.50	177669	20681	132	0.13
Ni	221.647	1.6	8829	555	67	0.81
Pb	220.353	2.6	6776	1356	250	0.34
Sb	206.833	5.4	1562	329	267	0.67
Se	196.026	13	471	200	431	1.01
Ti	334.941	0.075	360898	5963	17	0.15
U	367.007	0.47	74464	8083	122	0.13
V	309.311	0.39	246412	20670	92	0.14
Zn	213.856	0.35	59088	1211	21	0.56

[a] See footnotes to Table 2.

Table 4
Multielement detection limit data for Set 3 conditions, axial viewing with pneumatic nebulization and "robust" plasma conditions; an integration time of 10 s was used[a]

Element	λ/nm	DL/(ng ml^{-1})	z_a	z_b	BEC/(ng ml^{-1})	RSDB/%
As	189.042	10	3584	2020	1292	0.26
As	193.696	10	5915	3543	1494	0.23
Ba	455.403	0.043	3197090	254692	87	0.02
Be	313.042	0.019	6436437	147837	24	0.03
Cd	214.438	0.31	149901	10779	77	0.13
Cr	205.552	1.0	35401	6642	231	0.14
Cu	324.754	0.76	213161	93441	780	0.03
Fe	238.204	1.0	59140	10224	209	0.16
Mn	257.610	0.14	296095	14955	53	0.09
Mo	202.030	1.46	27606	6567	312	0.16
Na	589.592	2.8	371619	200290	1169	0.08
Ni	221.647	10.2	25966	5767	286	1.19
Pb	220.353	3.4	28793	16457	1334	0.08
Sb	206.833	17	4662	3341	2529	0.22
Se	196.026	15	2844	2003	1392	0.35
Ti	334.941	0.24	407857	66827	196	0.04
U	367.007	2.6	135573	99859	2796	0.03
V	309.311	0.60	389087	90728	304	0.07
Zn	213.856	0.47	105345	10779	114	0.14

[a] See footnotes to Table 2.

Table 5
Multielement detection limit data for Set 4 conditions, axial viewing with ultrasonic nebulization; an integration time of 10 s was used[a]

Element	λ/nm	DL/(ng ml^{-1})	z_a	z_b	BEC/(ng ml^{-1})	RSDB/%
As	189.042	0.74	5004	136	28	0.88
As	193.696	0.89	7418	235	33	0.91
Ba[b]	455.403	–	–	–	–	–
Be	313.042	0.001	34516508	29436	0.85	0.05
Cd	214.438	0.028	364619	852	2.3	0.40
Cr	205.552	0.068	197428	436	2.2	1.02
Cu	324.754	0.027	2151739	6249	2.9	0.31
Fe	238.204	0.29	260853	591	2.3	4.28
Mn	257.610	0.020	1740800	889	0.51	1.29
Mo	202.030	0.058	154362	426	2.8	0.70
Na	589.592	5.2	1946021	9365	4.8	35.75
Ni	221.647	0.072	80938	404	5.0	0.48
Pb	220.353	0.29	55182	1002	18	0.52
Sb	206.833	0.62	8714	201	24	0.88
Se	196.026	1.0	2428	141	36	0.92
Ti	334.941	0.042	3860840	3800	1.0	1.43
U	367.007	0.099	846377	6222	7.4	0.44
V	309.311	0.013	3240796	7504	2.3	0.19
Zn	213.856	0.083	453537	1151	2.5	1.08

[a] See footnotes to Table 2. [b] Extremely high intensity under these conditions prevented measurement.

used for the blank model collection. To obtain the detection limits, 30 replicate determinations were made while introducing a blank solution into the system.

2.4. SBR-RSDB approach

Detection limits were interpreted using the SBR-RSDB approach described in a tutorial by Boumans et al. [18,19]. In this work, the SBR was converted to background equivalent concentration (BEC) so as to make the expression independent of the standard concentration used.

The detection limit equation (Eq. (1)), gives the relationship between the detection limit (DL), BEC, and RSDB.

$$DL = 3 \times BEC \times 0.01 \times RSDB \tag{1}$$

The improvements to the detection limit from increased photon flux and longer integration times were revealed in an RSDB analysis. The RSDB equation used in this work is

$$RSDB = 100 \sqrt{\alpha^2 + \frac{\beta}{z_b \tau}\left[1 + \frac{z_d}{z_b}\right]} \tag{2}$$

In Eq. (2), RSDB is the relative standard deviation of the background signal expressed as percent (unitless), α is the flicker noise coefficient (unitless), β is the shot noise coefficient (counts per photoelectron), z_b is the net background intensity at peak maximum (counts s^{-1}), z_d is the magnitude of the dark current signal (counts s^{-1}), and τ is the integration time (s). The application of this equation has been previously demonstrated [17–19].

A simplified equation may be used to approximate the RSDB when some assumptions are made. Because background signal flicker noise was filtered out when detection limits were measured using MSF, α was set equal to zero [17]. A further simplification comes from the fact that the dark current of the detector was small relative to the background signals observed. Thus, the expression in square brackets in the shot noise term was assumed to be equal to unity. These assumptions lead to the simpler expression for the RSDB given in Eq. (3).

$$RSDB = 100 \sqrt{\frac{\beta}{z_b \tau}} \tag{3}$$

With MSF data processing, the detection limits were produced directly after the algorithm was invoked. Consequently, BEC and RSDB values were not provided directly. However, BEC values were easily obtained from a separate measurement to get raw intensities, and the RSDB was then generated by using Eq. (1) and solving the equation for the RSDB. This procedure has been found to give consistent interpretation of the detection limits [17] and is used routinely in our laboratory. To compare detection limit results from this work with other ICP systems which may not have simultaneous spectral readout, the value of α must be estimated and the RSDB recalculated using Eq. (2). Thus, the flicker noise component of the RSDB adds in quadrature with the shot noise component, and predictably higher values of the RSDB will result [17].

In Section 3.1, detection limit experiments conducted for a fixed set of 19 spectral lines under the four different sets of plasma conditions as outlined in Table 1 are described. The detection limit results and accompanying data for the four sets of conditions, Set 1, Set 2, Set 3, and Set 4, are provided in Tables 2, 3, 4, and 5 respectively. For Tables 2–5, the integration time τ was 10 s. In order to use the SBR-RSDB theory, a value was assigned to the shot noise coefficient β based on the empirical data. In Section 3.3, an integration time of 60 s was used for the detection limit experiments.

3. Results and discussion

3.1. Detection limits with pneumatic nebulization

3.1.1. Determination of the shot noise coefficient β

From Eq. (3), it was possible to generate an estimate for β from a single RSDB value. However, a more meaningful estimate arises from using as much of the RSDB data as possible. It was observed that, in addition to the natural variance associated with measurements of the RSDB, occasionally very high RSDB values were produced. Although these were few, including them in the overall calculation of β would have resulted in a biased estimate. High RSDB values may have resulted from detection of analyte during the blank measurement sequence. Such a situation may have come about as a consequence of a carryover problem. Because high

RSDB values resulted in high values of β, the outliers were identified in a frequency distribution.

In Fig. 1, the frequency distribution of β is shown over the 57 detection limit values taken from Tables 2–4. Table 5 data were not used due to a recognized carryover problem with the ultrasonic nebulizer setup discussed later in this section. Based on the frequency distribution in Fig. 1, β values higher than 0.3 were considered to be outliers. More than 80% of the data were used to calculate an average β value of 0.13 (counts per photoelectron). This value is close to that corresponding to the highest frequency of occurrence in Fig. 1. This method, although not mathematically rigorous, provided a useful number for β with which to characterize the shot noise nature of the RSDB. Shot noise follows a Poisson distribution [18]. The number of photoelectrons (photoelectrons are related to instrument readout counts in the following way: number of photoelectrons = (intensity as counts/s) × τ/β) recorded within the integration time interval for the weakest background signals is larger than 2000. At these levels, the Poisson distribution approaches a normal distribution with equal mean and variance [20]. Therefore, the chi-squared distribution can be used to estimate the variance of β. With a 99% confidence level and a mean value of $\beta = 0.13$, the upper confidence limit for β was 0.298. This provided a means to validate the value of 0.3 used as the cutoff. The estimate of $\beta = 0.13$ differs from a previously estimated value of $\beta = 0.087$ [17] owing to adjustment of the detector gain and setup voltages.

The RSDB data from Tables 2–4 were plotted as a function of background signal intensity in Fig. 2. Also plotted was the theoretical RSDB obtained using Eq. (3) with a value of $\beta = 0.13$ and the 99% confidence bands. Three data points were omitted from the plot because they were gross outliers. These were the values for Cr from Table 3, for Ni from Table 4 and for Na from Table 4. Roughly 20% of the RSDB values fell outside of the 99% confidence limits. This suggests that a source of error exists that is not explained by random chance. A possible source of positive deviations of the RSDB (and therefore β) is carryover, a discussion of which is provided in Section 3.2.2.

An important feature in all of the detection limits recorded using pneumatic nebulization was that the RSDB component of the detection limits approached the theoretical shot noise limit. The general agreement with theory for all three sets of experimental conditions exhibited in Fig. 2 is testimony to the usefulness of the SBR-RSDB approach. The three sets of conditions were very different in nature and yielded different detection limits, yet the outcome for the RSDB was predictable from knowledge of only the background intensity once β and the integration time were given.

As shown in prior work [17], shot noise limited detection limits were realized because of simultaneous spectral registration and the filtering of correlated flicker noise in the background

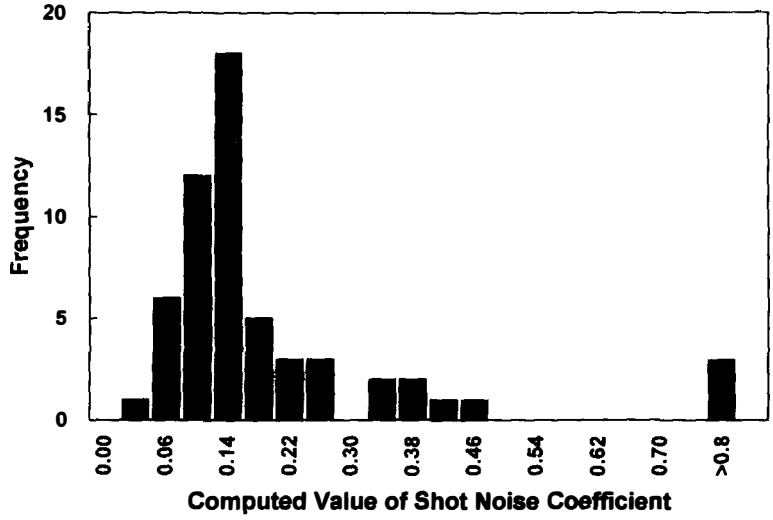

Fig. 1. Frequency distribution of β, the shot noise coefficient. Values of β are computed from individual detection limit values by first computing the RSDB from Eq. (1), then solving Eq. (3) for β. A bin size of 0.04 was used to prepare the frequency distribution plot. A value of $\beta = 0.13$ readout counts per photoelectron was assigned (see text).

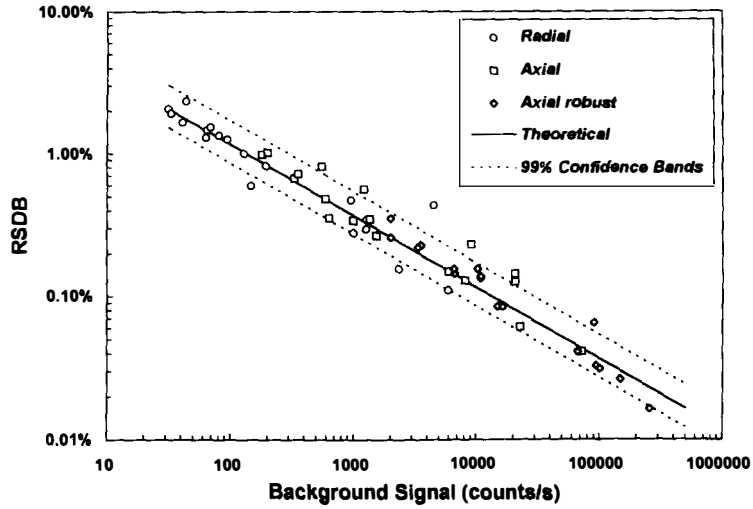

Fig. 2. A plot of RSDB vs. background signal for data collected with pneumatic nebulization. RSDB data from Tables 2, 3, and 4 are overlaid with the theoretical RSDB curve calculated using Eq. (3) and $\beta = 0.13$. The general agreement with theory is evidence that the RSDBs and detection limits approach values limited only by photon shot noise.

signal from MSF processing. Thus, photon shot noise was left as the principal source of noise in the RSDB. The correlation among uncorrected background signals at different wavelengths is illustrated in Fig. 3. Background signals at four wavelengths were monitored simultaneously by different subarrays. The noise in the four unmodified net background signals is dominated by multiplicative flicker noise and the signals were, therefore, tightly correlated as a function of time. An integration time of 100 s was used. The observation confirms that the noise correlation in background signals, already reported for radial viewing of the ICP [17, 21], was similarly observed for axial viewing.

3.1.2. Comparison of detection limit, BEC, and RSDB values

A comparison of the RSDB between radial (Set 1 conditions) and axial viewing (Set 2 conditions) was made. An average over all elements yielded an RSDB improvement of a factor

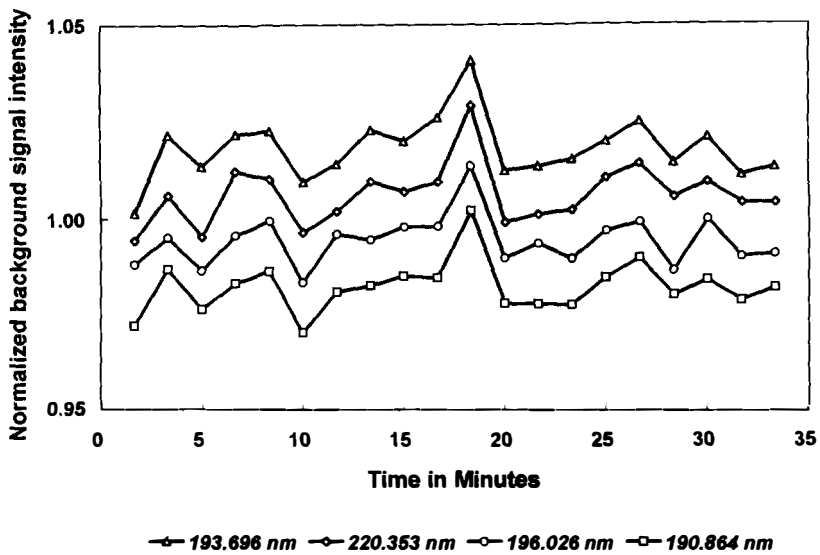

Fig. 3. Background signal record as a function of time from the axially viewed ICP. A 100 s integration time per point was used. The background signals at four different wavelengths were normalized to unity and offset slightly from each other for clarity. The signals were monitored simultaneously by different subarrays. Multiplicative flicker noise from the ICP source dominates the noise signature in the signal record. A high degree of noise correlation is observed. Multiplicative flicker noise is easily removed using the redundant sampling of the background signal provided by the simultaneous solid state detection system.

of about 2.5. The reason for the improvement was the factor of seven higher background intensity entering the spectrometer with the axial viewing setup. The RSDB improvement with increasing background level is initially counter-intuitive, but is easily understood from Eq. (3). The total background noise must increase as the background signal increases. However, the RSD of a shot noise limited background signal will become smaller as the signal increases in proportion to the inverse square root of the signal intensity. Hence, higher optical throughput improved the RSDB as predicted in Eq. (3). The RSDB improvement with axial viewing was observed in Fig. 2 as the RSDBs for the same 19 elements shifted to lower values when the corresponding background level increased.

Fortunately, the increase in background intensity with axial viewing was accompanied by a proportionately larger increase in the analyte signal intensities. On average, a factor of 13 improvement in the signal intensity was observed. After accounting for both the background and analyte intensity changes, the SBR (and the BEC) improved by about a factor of two. The increase in signals was attributed to the longer pathlength or increased observation volume obtained in the axial viewing configuration. The net BEC improvements resulted from a better SBR in the radial center of the plasma than when emission is viewed from the side.

The data in Tables 2 and 3 show a factor of five overall improvement in detection limits with axial viewing compared to radial viewing. The improvement, easily understood in the context of Eq. (1), came from the factor of 2.5 RSDB improvement and the factor of two BEC improvement. This analysis was repeated for the data in Table 4 which was collected with "robust" conditions and axial viewing (Set 3 conditions).

Detection limits with Set 3 conditions were slightly poorer than with the Set 2 conditions. For As, Be, Cd, Pb, Se, and Zn, there were either no degradations in detection limit or the differences were less than a factor of 1.5. For Cr, Cu, Fe, Mn, Mo, Sb and Ti, a factor of two to three detection limit degradations were observed with robust conditions. For Ba, Na, Ni and U, the degradations were between factors of three and six.

With Set 3 conditions, the increase in RF power to the ICP and the drop in nebulizer gas flow raised the background intensity by about a factor of ten. The emission from analyte species did not increase by such a large amount and the resulting degradation in BEC was around a factor of six. The RSDB, however, improved on average by about a factor of three because of the higher background intensity. This explains the average factor of two degradation in the detection limit observed over the whole set of elements. Nonetheless, Ba, Na, Ni, and U had noticeably larger degradations compared to the rest of the group. The elements Na and Ni were identified earlier as outliers in Table 4 because of their very high RSDB values. This may have been the result of a carryover problem. For Ba and U, the problem was a very high BEC degradation which remains unexplained.

3.2. Detection limits with ultrasonic nebulization

3.2.1. Comparison of results

Values for detection limits using Set 4 conditions (ultrasonic nebulization) are given in Table 5. The detection limits improved compared to Set 2 (pneumatic nebulization) conditions by a factor of ten. The main reason for the improvement was a large increase in analyte signal resulting from the high efficiency of ultrasonic nebulization [22–24]. The overall background intensity remained roughly the same. The BEC improvements ranged from a factor of 10–50. However, several of these BEC enhancements did not translate directly into detection limit improvements of the same magnitude because of degradation in the RSDB. Because the background intensity with ultrasonic nebulization remained similar to the pneumatic nebulizer data, an RSDB degradation was not expected. Nevertheless, departures from the expected RSDB values were observed. The RSDB results were plotted in Fig. 4 and compared to the theoretical line. In contrast to Fig. 2, the plot in Fig. 4 shows that many of the measured RSDB values fell well above theoretical expectation. This positive bias may have resulted from carryover. If analyte was detected during the blank measurements (when none was expected), then the RSDB increased and a degradation of the detection limit resulted. It was found that Na gave a very poor RSDB value. This was probably caused by the introduction of very high levels of Na during the matrix effect experiments with pneumatic nebulization which were performed

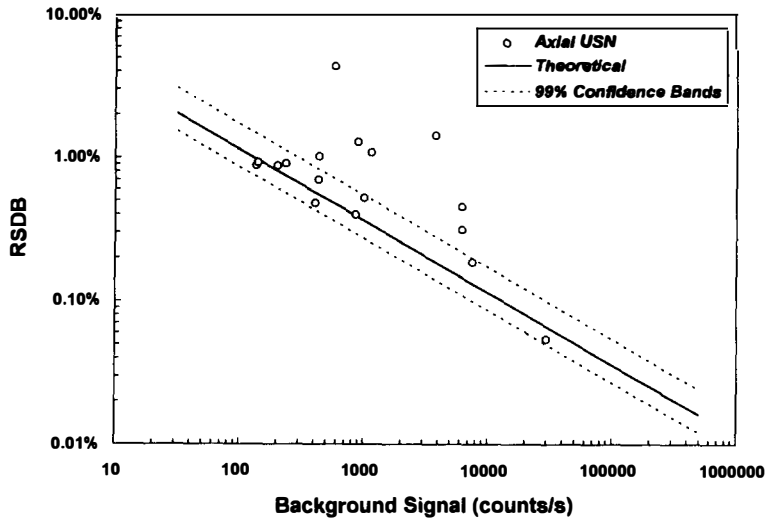

Fig. 4. A plot of RSDB vs. background signal for data collected with ultrasonic nebulization. RSDB data from Table 5 are overlaid with the theoretical RSDB curve calculated using Eq. (3) and $\beta = 0.13$. Compared to the pneumatic nebulizer data, a greater fraction of the RSDB values fall outside the 99% confidence intervals (see text).

prior to the ultrasonic nebulizer work. Because the torch assembly was exposed to very high levels of Na, poor detection limit performance for this element was anticipated. For this reason, Na was omitted from the RSDB plot in Fig. 4 and is not treated in further discussion.

3.2.2. Carryover problem

Despite efforts to maintain a clean sample introduction system, carryover of analyte material was a source of difficulty in the detection limit experiments. Carryover phenomena became much more significant when the detection power of the system was improved. This was particularly true of the results in which the ultrasonic nebulizer was coupled to the axially viewed ICP.

To determine if analyte signal was detected during the blank run, the MSF output for the analyte was examined for elements which exhibited high RSDB values. Two such elements were Fe and Ti. The analyte signal record as a function of read number for Fe and Ti was plotted in Fig. 5 for all 30 measurements of the blank solution in the detection limit experiment. For measurements of the blank solution, signal values should have been distributed around zero with deviations arising largely from noise in the measurement of spectra. However, it

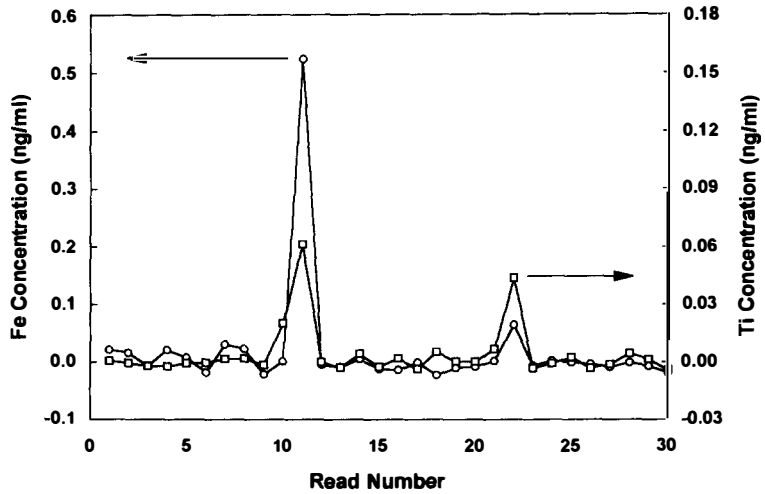

Fig. 5. Evidence of a carryover problem. The plot is the analyte concentration record for iron and titanium for the 30 replicate measurements of the blank solution made during the ultrasonic nebulizer detection limit experiments. Carryover of analyte material was recorded during reads 10, 11, and 22 for titanium and reads 11 and 22 for iron.

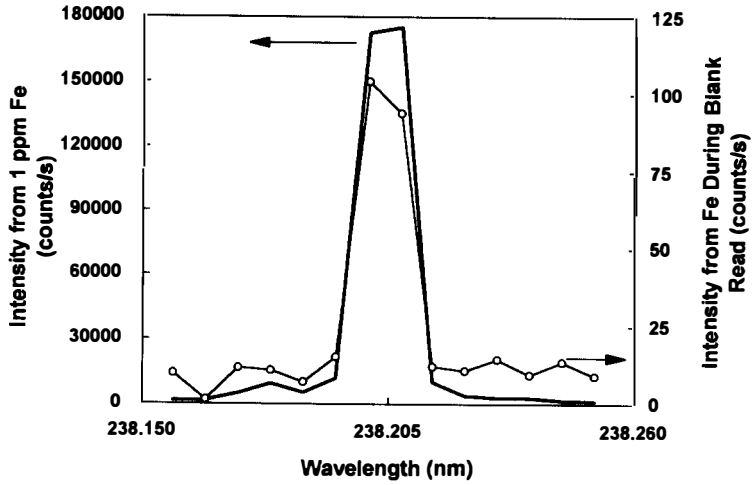

Fig. 6. Spectra of iron at 238.203 nm from the ultrasonic nebulizer detection limit experiment. The spectrum for a 1 ppm iron standard and the spectrum recorded during read 11 while aspirating the blank solution are overlaid for comparison. The detection of iron during measurement of the blank is confirmed.

was found that large deviations from the baseline noise were registered at reads 11 and 22 for both Fe and Ti. For Ti, read 10 also appeared to give a high value for the blank determination. The presence of the analyte was verified by examination of the spectrum for Fe at read number 11. This spectrum, plotted in Fig. 6, showed that Fe was clearly detected and that carryover or contamination was indeed the cause of the high RSDB. The simultaneous spectral output of the instrument was of paramount importance to understanding the source of the RSDB error and for unambiguous assignment of the observed signal to the presence of analyte and not a disruption in the background. The MSF output in Fig. 5 very clearly displayed the detection of analyte. The use of MSF removed the need for visual inspection of spectra in order to identify a carryover problem such as this one.

At the sub nanogram per millilitre level of detection obtained with the ultrasonic nebulizer setup, it was not entirely surprising that problems of carryover or contamination were more significant because the influence of these effects became more readily detectable. A likely scenario for the signal spikes was that sample particles had dislodged from an internal surface within the ultrasonic nebulizer, or perhaps from the aerosol delivery tube, and made their way to the ICP to finally be detected during reads 11 and 22. This may explain why the spikes were correlated for several elements.

As shown in Table 6, removal of the data points for reads 11 and 22 for Fe and reads 10, 11, and 22 for Ti, lead to RSDB and detection limit values very close to those which were predicted from Eqs. (1) and (3). Therefore, the carryover effect can be overcome and the detection limits for Fe and Ti would improve by an additional factor of seven and five respectively and the RSDB values would agree with theoretical prediction. Despite the difficulties in obtaining analyte-free blank measurements in this work, much of the detection limit advantage

Table 6
Ultrasonic nebulizer detection limit and RSDB data for Fe and Ti before and after removal of data points displaying a carryover problem[a]

Line	Results using all data			Results after selective data removal			
	DL/(ng ml^{-1})	BEC/(ng ml^{-1})	RSDB/%	DL/(ng ml^{-1})	BEC/(ng ml^{-1})	RSDB/%	$RSDB_{theory}$/%[b]
Fe 238.204 nm	0.29	2.3	4.28	0.042	2.3	0.61	0.47
Ti 334.941 nm	0.042	1.0	1.43	0.009	1.0	0.29	0.18

[a] Of the 30 reads taken during the detection limit experiment, reads 11 and 22 were removed for Fe. Reads 10, 11, and 12 were removed for Ti (see Fig. 5 and text). The RSDB data approach the theoretical prediction after the selective data removal. [b] Theoretical RSDB calculated from Eq. (3) with $\beta = 0.13$ and $\tau = 10$ s.

of the ultrasonic nebulizer was retained with axial viewing. The improvement factors observed in this work were similar to those reported previously in the literature for radial viewing of the ICP [22–25].

3.2.3. SBR-RSDB approach as a diagnostic tool

An important advantage of the SBR-RSDB approach and its value as a diagnostic tool has thus been demonstrated. The integrity of a multielement blank measurement with the ICP can be quickly evaluated by an examination of the RSDB graph. The information conveyed in RSDB analyses can be used routinely in the laboratory to evaluate the quality of detection limit data and to insure proper instrument function. This can be accomplished by the comparison of experimental results with theoretical expectation as discussed above. Once the value of the shot noise coefficient β has been established for a given instrument, the theoretical RSDB and detection limit can be computed from only the analyte signal and the background signal intensities. (The value of the flicker noise coefficient α would also be needed if the instrument uses sequential measurement procedures for background correction.) In this case, the SBR-RSDB approach was successfully used to expose and isolate a carryover problem in a directed manner.

3.3. The role of integration time

Further advantage can be taken of the knowledge that detection limits were shot noise limited and that they are generally predictable from Eqs. (1) and (3). From Eq. (3) it is clear that integration time can be increased to improve the detection limits in proportion to the inverse square-root of the integration time. An experiment was conducted to observe this effect. Detection limits were measured using a 60 s sampling time for the elements As, Se, Pb, and Tl. These four elements were chosen because of their importance in environmental applications and because they are part of a group considered to be a "weak" spot of ICP performance in which higher detection power is desired [26]. The detection limit results in Table 7 were obtained using Set 1, Set 2, and Set 4 conditions. The six-fold increase in integration time, compared to the 10 s data in Tables 2–5, was predicted to give an improvement factor of about 2.4 (square root of 6). The results are in good agreement with this prediction. Thus, a significant advantage of shot noise limited detection limits was the ability to trade off analysis time for detection power. In practice, the upper boundary for the integration time was limited only by the time available to perform the analysis of interest. Finally, it was observed that the factor of five improvement for axial viewing compared to radial viewing was preserved. The roughly ten-fold improvement obtained with the use of the ultrasonic nebulizer was also retained in these experiments.

3.4. Radial emission profiles

As described in the Experimental section, an alignment of the viewing position in both horizontal and vertical directions was required for axial viewing. When Mn was used as the alignment element, the highest analyte emission point always coincided with the position giving the minimum background emission. Similar reports have been published in the literature for axial viewing [3–6]. Thus, the SBR was easily optimized. For many spectral lines it was found

Table 7
Detection limits in ng ml^{-1} (3σ) obtained using a 60 s integration time[a]

Element	λ/nm	Radial (Set 1)	Axial (Set 2)	Axial USN (Set 4)
As	193.696	13	2.0	0.34
Pb	220.353	5.6	0.8	0.061
Se	196.026	22	4.7	0.64
Tl	190.864	19	3.0	0.26

[a] Detection limits are observed to improve by the inverse square-root of integration time because the RSDB is shot noise limited (see Fig. 2 and text).

that radial plots of the signal to background gave a smooth curve with a well defined maximum in the center of the central channel. However, this was not the case with Se at the 196.026 nm line. In Fig. 7, the radial signal to background profiles for the Se 196.026 nm and Mn 257.610 nm lines are compared. The Se profile shows that emission is strongest at two local maxima around 1 mm off-axis with a depression of the SBR at the center of the axial channel. This contrasts with the Mn profile which exhibits a single central maximum.

The information available in Fig. 7 was not sufficient to draw an unequivocal conclusion. However, a proposed explanation for the appearance of the Se radial profile is that the shape is being strongly influenced by the radial excitation temperature profile in the ICP. The upper level of the Se transition is of higher excitation energy (6.32 eV) compared to that for the Mn transition (4.81 eV). The difference in the profile shapes between Se and Mn was a result of the excitation energy difference between these two transitions. It has been shown that excitation temperatures can peak off-axis from the central channel in regions between the normal analytical zone and the fireball within the load coil [6,27–30]. The asymmetry in the observed profiles in Fig. 7 was the manifestation of the asymmetry in the radial temperature profiles as has been illustrated in tomographic studies of the ICP by Hieftje [31]. Asymmetric excitation temperature profiles with axial viewing have been previously reported by de Loos-Vollebregt et al. [6].

3.5. Analytical precision

Precision experiments were undertaken with the radially and axially viewed plasma. All measured values of the precision as percent relative standard deviation were less than 1%, with most values less than 0.5% for the lines tested. The precision results using Set 1, Set 2, and Set 4 conditions are presented graphically in Fig. 8. The 95% confidence bands for the RSD values are shown with error bars. A rigorous statistical treatment was not warranted but the differences in precision were observed to be small with the possible exception of Zn at 213.856 nm with the ultrasonic nebulizer. The element lines were chosen according to guidelines in the drift diagnostics suggested by Carré et al. [12] and Poussel et al. [13]. These four lines span a large range of excitation energy and ionization energy. It was not clear if the observed differences in precision were related to line character. Nonetheless, it was likely that the dominant source of the noise for these signals originated in the fluctuations occurring in the generation and transport of sample aerosol [21,30]. At an integration time of 10 s, the processes sampled were very slow by comparison to the millisecond transit times of sample particles in the torch. Therefore, little difference in precision between the two viewing modes

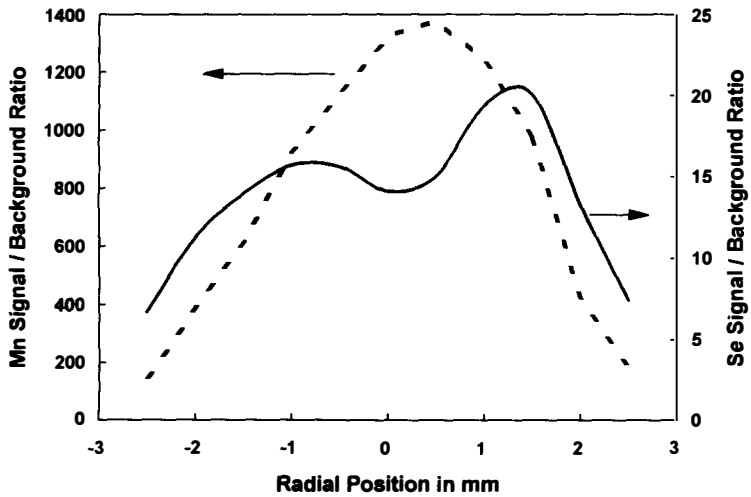

Fig. 7. Radially resolved signal to background ratio plots for the Mn 257.610 nm and Se 196.026 nm lines. The axially viewed ICP was used with pneumatic sample nebulization. The Mn signal to background ratio is observed to have a single maximum at the central channel whereas the Se signal to background ratio profile exhibits two asymmetric, off-axis maxima.

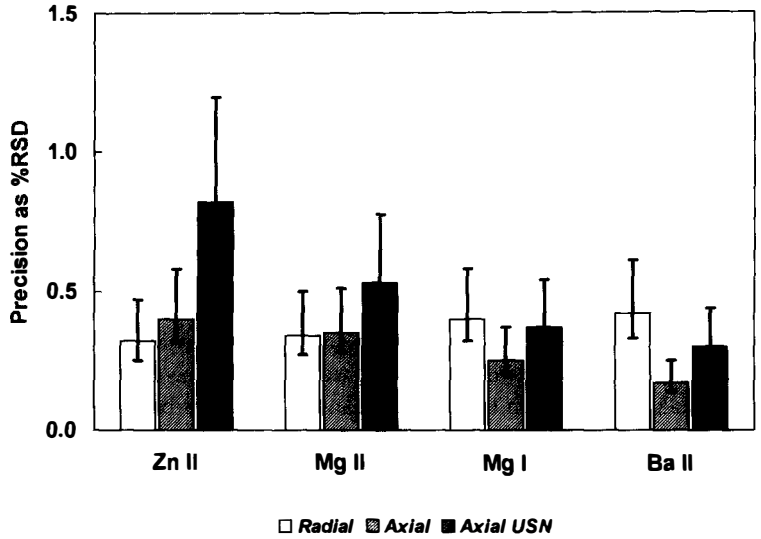

Fig. 8. Comparison of analytical precision as percent RSD for three different conditions labeled Radial (Set 1 conditions), Axial (Set 2 conditions) and Axial USN (Set 4 conditions). The error bars show the 95% confidence interval associated with each precision measurement. Except for the Zn value with the Axial USN system, precision values are similar for the different elements and sets of conditions.

was expected in these experiments from the spatial averaging of the central channel by the imaging optics combined with the temporal averaging of the integration time used for detection.

3.6. Linear working range for Cd

The instrument response as a function of concentration was measured for both the axial and radial viewing arrangements using two Cd lines. The concentrations of Cd used were 0.1, 1, 10, 100, 1000, and 10 000 μg ml^{-1}. Plots of the instrument response as a function of concentration were given for Cd (I) at 228.802 nm and 361.051 nm in Figs. 9 and 10 respectively. The instrument response was calibrated to the peak intensity obtained with the 1 μg ml^{-1} solution of

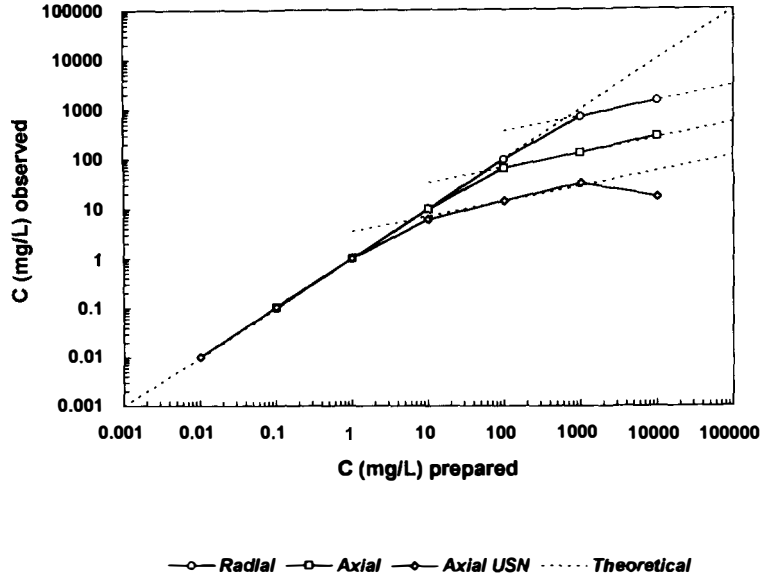

Fig. 9. Linearity plots for Cd (I) at 228.802 nm, a relatively strong, resonance transition. The instrument response as a function of Cd concentration was normalized at 1 μg ml^{-1}. Self-absorption causes the instrument response to depart from a linear relationship in a way that is dependent on experimental conditions. The dotted lines represent theoretical asymptotic lines of slope unity in log–log space (optically thin system) or of slope ½ in log–log space (system with high optical thickness).

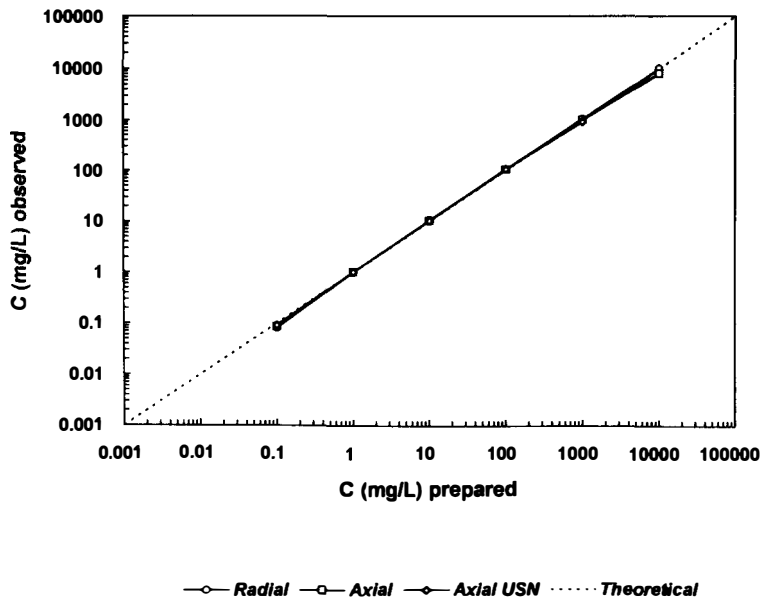

Fig. 10. Linearity plots for Cd (I) at 361.051 nm, a relatively weak, non-resonance transition. The instrument response as a function of Cd concentration was normalized at 1 μg ml^{-1}. The instrument response is linear over the concentration range examined and self-absorption was not observed. The dotted line represents the theoretical line of slope unity in log–log space (optically thin system).

Cd. The ordinate was then represented in observed concentration units. No corrections were made for possible matrix effects which may occur at high concentrations of Cd. However, the data for the Cd 361.051 nm line indicate that little or no matrix effects were observed at this wavelength.

The effects of self-absorption are most pronounced for emission lines whose transitions involve the ground state of the emitting species [32]. The Cd 228.802 nm line is a resonance line and makes a good test case for observing self-absorption. In contrast, the Cd 361.051 nm line is not a resonance line and has a much weaker transition probability compared to the 228.802 nm line. The different behavior of these two lines is apparent in Figs. 9 and 10. At high Cd concentrations, the 228.802 nm line exhibited deviations from linearity at different concentrations depending on the conditions and experimental setup, whereas there was little or no curvature of the working curve for the 361.051 nm line. This illustrates the usefulness of ICP instrumentation with multiline capability which can take advantage of the properties of different lines.

The curvature observed for the Cd 228.802 nm data in Fig. 9 was a result of self-absorption. The concentration point at which there was a departure from linearity occurs at different concentrations for the three different experimental setups. This was explained by the fact that the point of departure from linearity was related to the number of free atoms which were excited n_i within the volume of observation [32]. With axial viewing, the pathlength of observation in the plasma was longer compared to radial viewing. Therefore, for the same concentration of analyte n_i increased with axial viewing and the point of departure from linearity moved to lower concentration. When the ultrasonic nebulizer was used, a higher mass of analyte was transported into the ICP compared to that for pneumatic nebulization (discussed above). This increased the value of n_i and further lowered the concentration point at which the departure from linearity occurred.

A logarithmic transformation of the linearity data shown in Fig. 9 indicates that the data initially follows a line of slope unity (in log–log space) at low concentrations. At the high concentration end, the data approached a limiting slope of $\frac{1}{2}$. The region where the line has a slope of unity is characterized by the assumption of an optically thin system [33]. In the case of high optical thickness, an asymptotic limiting slope of $\frac{1}{2}$ is expected from the theory of thermal emission of homogeneous temperature sources [32]. The dotted lines in Fig. 9 have slopes of either unity or $\frac{1}{2}$ and represent the expected limiting slopes according to theory. The

data largely follow the theoretical trends, but a sharp departure occurred for the datum point at 10 000 μg ml^{-1} Cd with the ultrasonic nebulizer. This datum point reflects the breakdown of the assumption of a homogenous source. This datum represents the highest value of n_i in the data set. Here, the spectral line has undergone extreme self-absorption to the point of self-reversal.

Finally, attaching a value to the linear range in terms of orders of magnitude involved the definition of the endpoints of the linear curve. In this work, the low concentration end was considered bounded by the detection limit (defined above). The high concentration boundary was defined as the point of departure from a slope of unity in log–log space and was identified by the intersection of the theoretical line of slope unity and the asymptotic line of slope ½. By casting the axes of the linearity plot in units of the concentration to detection limit ratio, the linear range for all three experimental setups can be read off the graph in Fig. 11. It is observed that all three experimental conditions give very similar linear ranges. The linear range of the Cd 228.802 nm line expressed as order of magnitude (logarithm of the concentration to detection limit ratio) was about 5.5 orders for radial viewing and 5.0 orders for axial viewing (regardless of whether pneumatic or ultrasonic nebulization was used). The fact that there was little overall difference among the three sets of experimental conditions suggests that the shear gas was effective in minimizing the effect of self-absorption in the axial viewing arrangement. These results are in agreement with the work of Demers [3] and confirm that axial viewing shifted the linear range to lower concentrations while retaining a similar span in concentration as radial viewing.

3.7. Molecular spectra from OH

It was observed that OH bands were more intense relative to the argon continuum background. This is visible in the spectra plotted in Fig. 12 for V at 309.311 nm. Using the blank spectra, the peak OH SBR was increased by a factor of about three for the axial setup compared to the radial setup. Thus, it was not surprising that the BEC for V 309.311 nm degraded with axial viewing owing to the larger molecular interference. The BEC degradation resulted in only a factor of two improvement in detection limit for V (see Tables 2 and 3) compared to the average factor of five improvement.

The reason for the increased molecular emission was probably that emission from OH mol-

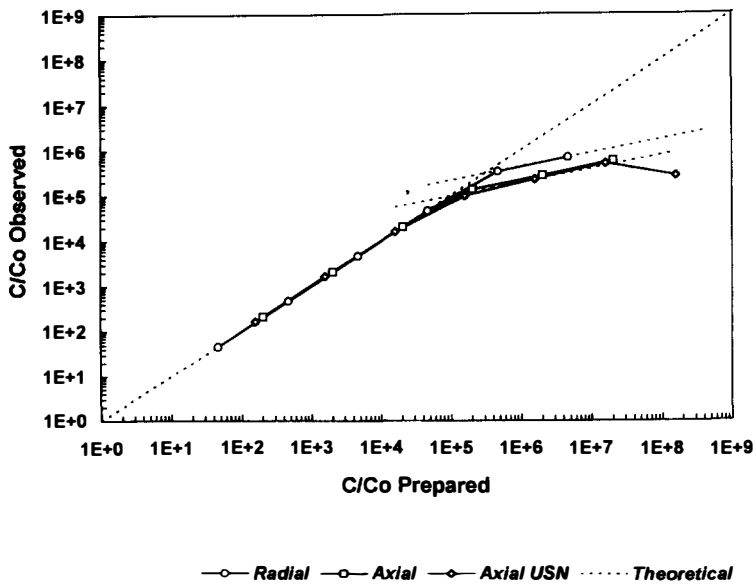

Fig. 11. The data plotted in Fig. 9. are replotted here in terms of concentration to detection limit ratios. This presentation makes it possible to read the true linear range directly from the graph. The differences noted in Fig. 9. are not present in this format. This indicates that very similar linear working ranges are observed for the three different experimental arrangements.

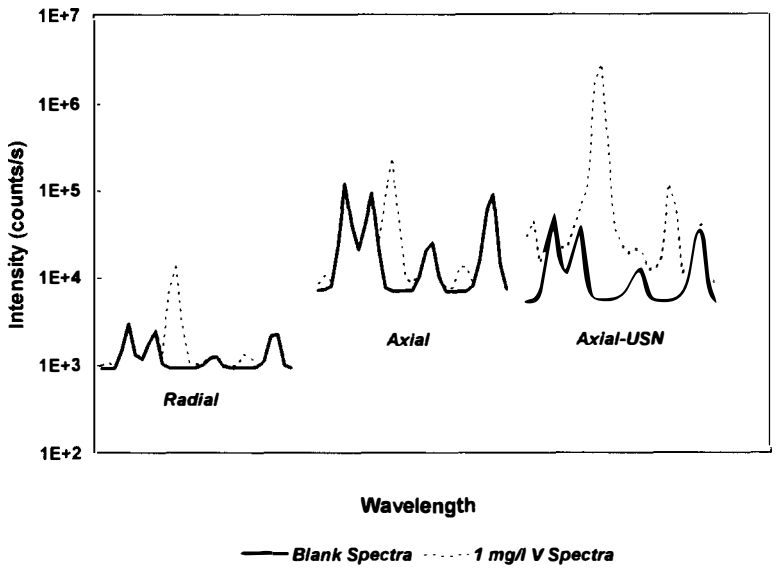

Fig. 12. Comparison of spectra from the subarray corresponding to V (II) at 309.311 nm. These spectra span 0.3 nm in wavelength and contain OH molecular band structure in the background. An increase in OH band emission is observed with axial viewing compared to radial viewing. The desolvation stage of the ultrasonic nebulizer (USN) helps to reduce OH emission compared to conventional pneumatic nebulization.

ecules, originating from droplets in the central channel, was sampled more efficiently with the axial viewing arrangement compared with radial viewing. Furthermore, emission from the extreme, cooler regions of the plasma, where the population of OH may be higher, was allowed to enter the spectrometer. When the ultrasonic nebulizer was used, a slight reduction in the OH emission was observed even though the analyte transport efficiency of this nebulizer was a factor of ten higher than pneumatic nebulization. The desolvation stage of the ultrasonic nebulizer is an important factor here because removal of water from the sample aerosol stream is expected to reduce the magnitude of OH emission. It may be possible to reduce the levels of molecular emission with the axially viewed ICP and pneumatic sample introduction by using a desolvation stage. A convenient means to achieve this might be with a Nafion drying tube attached to the output of the spray chamber [34].

3.8. Matrix effects

The suppression of analyte line signals in the presence of 10% w/v NaCl was measured for three sets of conditions. Matrix effects were compared for Set 1, Set 2, and Set 3 conditions. Table 8 contains the peak signal intensities for each line with and without the 10% NaCl matrix. The spectral lines chosen for the comparison again follow Mermet and co-workers' suggestions [12,13]. These lines were useful because they spanned a large range of energy sums (defined as excitation energy + ionization energy). The amount of signal suppression is tabulated as percent change of the signal when NaCl was present. Also shown in Table 8 is the Mg (II) 280.273/Mg (I) 285.213 nm ratio (Mg (II)/(I) ratio) corrected for the differences in echelle grating efficiency. The grating efficiency difference is compensated by applying a factor of 1.85 to the Mg (II)/(I) ratio.

Ion line signal suppressions when NaCl was present were nearly a factor of two more severe with axial viewing. A trend towards greater signal suppression was observed for lines with higher energy sums. The Zn (II) 206.200 nm line (highest energy sum in the group) always exhibited the largest suppressions and the Mg (I) 285.213 nm line (lowest energy sum) always had the least suppression. Hence the influence of matrix effects from a high Na matrix are dependent on line character in a similar way with either radial or axial viewing, but the magnitudes of the effects are greater for axial viewing.

The Mg (II)/(I) ratio increased for axial viewing when no NaCl was present. Based on experiments with radial viewing [11], this could be assumed to indicate a more robust plasma.

Table 8
Effect of 10% w/v NaCl on peak emission signals[a]

Species	λ/nm	E_{sum}/eV[b]	Radial (Set 1 conditions)			Axial (Set 2 conditions)			Axial robust (Set 3 conditions)		
			Intensity no NaCl	Intensity 10% NaCl	Change/%	Intensity no NaCl	Intensity 10% NaCl	Change/%	Intensity no NaCl	Intensity 10% NaCl	Change/%
Zn (II)	206.200	15.40	13673	5429	−60	227811	44737	−80	1259142	617957	−51
Mg (II)	280.270	12.07	51604	27208	−47	852915	259709	−70	1422710	871583	−39
Mg (I)	285.213	4.35	18334	13973	−24	265743	237483	−11	361734	275347	−24
Ba (II)	455.403	7.93	147368	92959	−37	1814619	637632	−65	1760226	997260	−43
Mg (II)/(I)[c]	–	–	5.2	3.6	−31	5.9	2.0	−66	7.3	5.9	−19

[a] The influence of the matrix was greater with axial viewing compared to radial viewing using the same RF power and nebulizer gas flow rate; however, robust conditions greatly lessened the degree of suppression for ion lines. [b] The E_{sum} values are the sum of the excitation and ionization energies as tabulated by Carré et al. [12]. [c] The Mg (II)/(I) ratio is corrected for differences in echelle grating efficiency.

However, results from the introduction of the NaCl solution show that this is not the case because the Mg (II)/(I) ratio is more severely affected in the axial viewing setup. Thus, it was clear from these experiments that the Mg (II)/(I) ratio may not be directly compared for the two different viewing arrangements.

Nevertheless, the trends with Mg (II)/(I) ratio and signal suppression with NaCl for a given viewing setup were retained. This was evident in the comparison between Set 2 and Set 3 conditions with the axial viewing setup. In Table 8, the same trend was observed for axial viewing as was described by Mermet [11] for radial viewing. With robust conditions (Set 3), the RF power was increased and the nebulizer flow was reduced. The resulting Mg (II)/(I) ratio for no NaCl is higher than that for typical conditions and the suppressions in the presence of NaCl are lessened. Thus, Set 3 conditions may be used to improve the suppression problem with axial viewing and achieve a level of robustness similar to or exceeding that observed in the radial viewing data (Set 1 conditions). Similarly, it is likely that reports of improved matrix effects with an axially viewed low-flow torch [6] were the result of the improved robustness gained from the use of a much lower nebulizer gas flow rate. Although not investigated here, it is expected from the work of Mermet [11] that radial viewing with robust conditions would provide the best experimental arrangement for minimization of the matrix effects described above.

4. Conclusions

The axially viewed horizontal ICP studied in this work provided a general improvement in detection limits of about a factor of five compared to radial viewing. This held true for a wide range of spectral lines. The improvement with axial viewing came partly from the high optical throughput (improves RSDB) and partly from the better SBRs (improves BEC) as compared to normal radial viewing. The RSDB and detection limit values were observed to follow the theoretical shot noise prediction.

The SBR-RSDB approach is an important tool for understanding detection limit differences and for identification of a carryover problem with the ultrasonic nebulizer. A key result was that the shot noise coefficient was constant for a given instrument and not dependent on sample introduction, viewing arrangement, or plasma torch parameters. Therefore, this method serves as a valuable diagnostic for quality control which can be applied routinely in the laboratory. In this work, the coupling of simultaneous spectral registration and MSF led to RSDB values which were only dependent on the shot noise coefficient, the intensity of the background, and the integration time. The precision of the analytical signals is similar for both viewing arrangements.

The linear dynamic range for the Cd 228.802 nm line with axial viewing was similar to radial viewing but shifted to lower concentration values. Increased self-absorption was responsible for reducing the high concentration side of the linear range by about an order of magnitude but this was largely compensated by the improvement in detection limits at the low concentration end. The data followed expected theoretical trends for lines undergoing self-absorption. The Cd 361.051 nm line was linear throughout the concentration range tested (up to 10 000 $\mu g\ ml^{-1}$).

Matrix effects caused by 10% w/v NaCl were found to be more severe with the axial viewing arrangement. Larger suppressions were found for ion lines with higher energy sums. The suppressions were reduced by using robust conditions. Although Mg (II)/(I) ratios were found to be higher with axial viewing, this did not indicate improved robustness with respect to matrix effects. It was concluded that the Mg (II)/(I) ratio could not be directly compared for the two viewing arrangements. However for a fixed viewing arrangement, all the expected trends were observed.

Molecular emission from OH was a factor of three more intense relative to the background with axial viewing. The elevation of molecular emission will have a detrimental impact on detection limits if the analyte emission peak is within a spectral region of molecular bands. Although not investigated in this report, molecular emission is expected to be more troublesome with organic sample introduction and axial viewing.

The overall analytical performance of the axially viewed plasma indicates that it may be

most successfully used when lower detection limits are desired. However, reduced plasma robustness and limitations at high concentrations for some analytes must be considered as trade-offs. For applications which involve samples with relatively high levels of matrix constituents, robust conditions can be used to alleviate matrix effects but not without a slight degradation in detection power (factor of two worse).

Finally, the use of ultrasonic nebulization with the axially viewed ICP gave an overall factor of 50 improvement in detection power over conventional radial viewing with pneumatic nebulization. The characteristic improvement in SBRs with ultrasonic nebulization was similar for either radial or axial viewing.

Acknowledgments

We thank Thomas Barnard of Perkin-Elmer and Walter Slavin of Bonaire Technologies for many helpful discussions and for constructive criticism of this manuscript. We also thank Cindy Anderau, a colleague at Perkin-Elmer, for her collaboration on the experiments related to the radial emission profiles of the ICP.

References

[1] M.H. Abdallah, R. Diemiaszonek, J.J. Jarosz, J.M. Mermet, J. Robin and C. Trassy, Anal. Chim. Acta, 84 (1976) 271.
[2] F.E. Lichte and S.R. Koirtyohann, ICP Information Newslett., 2 (1976) 192.
[3] D.R. Demers, Appl. Spectrosc., 33 (1979) 584.
[4] L.M. Faires, T.M. Bieniewski, C.T. Apel and T.M. Niemczyk, Appl. Spectrosc., 39 (1985) 5.
[5] J. Davies, J.R. Dean and R.D. Snook, Analyst, 110 (1985) 535.
[6] M.T.C. de Loos-Vollebregt, J.J. Tiggelman and L. de Galan, Spectrochim. Acta Part B, 43 (1988) 773.
[7] M.T.C. de Loos-Vollebregt, J.J. Tiggelman, P.C. Bank and C. Degraeuwe, J. Anal. At. Spectrom., 4 (1989) 213.
[8] Y. Nakamura, K. Takahashi, O. Kujirai, H. Okochi and C.W. McLeod, J. Anal. At. Spectrom., 9 (1994) 751.
[9] T.W. Barnard, M.I. Crockett, J.C. Ivaldi and P.L. Lundberg, Anal. Chem., 65 (1993) 1225.
[10] T.W. Barnard, M.I. Crockett, J.C. Ivaldi, P.L. Lundberg, D.A. Yates, P.A. Levine and D.J. Sauer, Anal. Chem., 65 (1993) 1231.
[11] J.M. Mermet, Anal. Chim. Acta, 250 (1991) 85.
[12] M. Carré, E. Poussel and J.M. Mermet, J. Anal. At. Spectrom., 7 (1992) 791.
[13] E. Poussel, J.M. Mermet and O. Samuel, Spectrochim. Acta Part B, 48 (1993) 743.
[14] B.L. Sharp, J. Anal. At. Spectrom., 3 (1988) 613.
[15] J.C. Ivaldi, J. Vollmer and W. Slavin, Spectrochim. Acta Part B, 46 (1991) 1063.
[16] J.C. Ivaldi, D. Tracy, T.W. Barnard and W. Slavin, Spectrochim. Acta Part B, 47 (1992) 1361.
[17] J.C. Ivaldi and T.W. Barnard, Spectrochim. Acta Part B, 48 (1992) 1265.
[18] P.W.J.M. Boumans, Spectrochim. Acta Part B, 46 (1991) 431.
[19] P.W.J.M. Boumans, J.C. Ivaldi and W. Slavin, Spectrochim. Acta Part B, 46 (1991) 641.
[20] G. Box, W. Hunter and J. Hunter, Statistics for Experimenters, Wiley, New York, 1978, pp. 118–145.
[21] S.A. Myers and D.H. Tracy, Spectrochim. Acta Part B, 38, (1983) 1227.
[22] K.W. Olsen, W.J. Haas, Jr and V.A. Fassel, Anal. Chem., 49 (1977) 632.
[23] P.W.J.M. Boumans and F.J. de Boer, Spectrochim. Acta Part B, 30 (1975) 309.
[24] P.W.J.M. Boumans and F.J. de Boer, Spectrochim. Acta Part B, 31 (1976) 355.
[25] V.A. Fassel and B.R. Bear, Spectrochim. Acta Part B, 41 (1986) 1089.
[26] P.W.J.M. Boumans, J. Anal. At. Spectrom., 8 (1993) 767.
[27] D.J. Kalnicky, R.N. Kniseley and V.A. Fassel, Spectrochim. Acta Part B, 30 (1975) 511.
[28] N. Furuta and G. Horlick, Spectrochim. Acta Part B, 37 (1982) 53.
[29] J.W. Olesik and S.J. Den, Spectrochim. Acta Part B, 45 (1990) 731.
[30] J.C. Fister III and J.W. Olesik, Spectrochim. Acta Part B, 46 (1991) 869.
[31] G.M. Hieftje, Spectrochim. Acta Part B, 47 (1992) 3.
[32] J.D. Ingle, Jr. and S.R. Crouch, Spectrochemical Analysis, Prentice Hall, New Jersey, 1988, pp. 214–217.
[33] M. Miller, Basic Concepts in Atomic Emission Spectroscopy, in A. Montaser and D.W. Golightly (Eds.), Inductively Coupled Plasmas in Analytical Atomic Spectrometery, VCH, New York, 1992, pp. 62–83.
[34] N.G. Sundin and J.F. Tyson, Spectrochim. Acta Part B, 50 (1995) 369.